Solar Energy Materials & Solar Cells 165 (2017) 94–102

Contents lists available at ScienceDirect

Solar Energy Materials & Solar Cells

journal homepage: www.elsevier.com/locate/solmat

Impact of front-side point contact/passivation geometry on thin-film solar cell performance

Giovanna Sozzi[a,*], Simone Di Napoli[a], Roberto Menozzi[a], Benjamin Bissig[b], Stephan Buecheler[b], Ayodhya N. Tiwari[b]

[a] Department of Engineering and Architecture, University of Parma, Parco Area delle Scienze 181A, 43124 Parma, Italy
[b] Laboratory for Thin Films and Photovoltaics, Empa - Swiss Federal Laboratories for Materials Science and Technology, Ueberlandstrasse 129, CH-8600 Duebendorf, Switzerland

ARTICLE INFO

Keywords:
Thin film CIGS solar cells
Surface passivation
Point contact
Numerical simulations
Buffer layer
Grain-Boundary

ABSTRACT

In this work, we perform an extensive campaign of three-dimensional numerical simulations of CIGS solar cell structures to investigate the effect of a surface-passivated CIGS with point contacts openings on the cell performance parameters (J_{sc}, V_{oc}, FF and η). Detailed analysis of the combination of passivation thickness, point contact size and pitch is performed under the hypothesis of highly defective CIGS front surface and ideal chemical passivation: efficiencies close to the case of ideal (i.e., defect-free) CdS/CIGS interface can be achieved by optimized nanometer-scale point contact arrays. To account for field-effect passivation due to positive residual charge density, Q_f, within the passivation layer, we vary Q_f in the range 10^{10}–10^{13} cm^{-2} under the two extreme scenarios of ideal or ineffective chemical passivation. Several examples of CIGS cells with different buffer layers (CdS, ZnO, ZnMgO, In_2S_3, Zn(O, S)) are also analyzed. We find that a positive Q_f in the interval 10^{12}– $5{\cdot}10^{12}$ cm^{-2} can help completely recover the ideal cell efficiency, irrespective of the chemical passivation effect and even in the presence of unfavorable conduction band alignment at the buffer/CIGS heterojunction. This may help devising solutions with buffer materials alternative to CdS, boosting the performance of otherwise surface-limited cells. The effect of grain boundary defect density and position with respect to point contacts is also addressed, with a grain dimension of 750 nm.

1. Introduction

Improvement in conversion efficiency of $Cu(In_{1-x}Ga_x)Se_2$ (CIGS) solar cells has been steady and remarkable, with laboratory-scale CIGS cells reaching efficiencies above 20% on a polyimide substrate [1] and beyond 22% [2,3] on soda-lime glass, thus exceeding those of other thin-film technologies. Improving conversion efficiency is essential to foster the competitiveness of photovoltaics in the energy market, and requires that the main performance-limiting electrical and optical loss mechanisms be identified so that, in a second step, researchers and manufacturers can devise solutions to overcome these limits. Major electrical losses in the cell are non-radiative bulk and interface recombination, which are therefore among the first and foremost performance limiters to take care of.

Record cells [1–3] feature a CdS buffer deposited by chemical bath to ensure suitable interface quality and favorable band-alignment at the CdS/CIGS interface, which results in low recombination rate through the inversion of CIGS surface, so that the cell should be limited by bulk properties, according to [4,5]. The assumption that interface recombination does not play a major role in CIGS solar cells with CdS buffer layer is also supported by several publications discussing the transport mechanism in CIGS solar cells (e.g., [6]). Applying this interpretation to the measured values of the parameters in the one diode model will result in the conclusion that interface recombination is not dominant. However, Scheer showed that interface recombination can be still the dominant mechanism even if the measured activation energy for J_0 is equal or close to the value of the energy band gap of the absorber [7]. Furthermore, the improvements obtained with the recently introduced alkaline post deposition treatment, which affects the interface between CIGS and buffer layer, strongly support the assumption that interface recombination is still limiting the device performance [8].

At the same time the interest in Cd-free buffer layers has been continuously growing, with the twofold purpose of reducing the absorption losses in the short wavelength range caused by the relatively low optical band gap of CdS (2.4 eV), and disposing of toxic Cadmium:

* Corresponding author.
E-mail address: giovanna.sozzi@unipr.it (G. Sozzi).

http://dx.doi.org/10.1016/j.solmat.2017.02.031
Received 23 September 2016; Received in revised form 17 January 2017; Accepted 22 February 2017

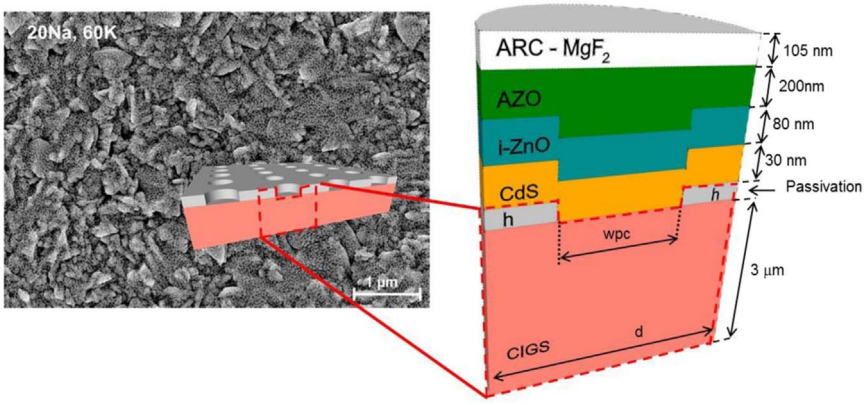

Fig. 1. Left: SEM micrograph of CIGS nano-patterned surface (after [26], supporting information); right: schematic cross-section of the 3D simulated cell.

alternative buffer materials with higher bandgap than CdS are available (the best alternatives being the ZnO-based compounds like Zn(O,S), ZnMgO and ZnSnO and the In_2S_3 [9–12]), but the quality of the interface with CIGS and of electron transport across the hetero-interface are often insufficient to provide efficiencies higher or even comparable with those of CdS-buffer cells [13,14].

Especially in the presence of sub-optimum buffer/absorber interface, the introduction of surface passivation and point contacts might help boost the cell performance, similarly to the case of advanced PERC cells [15] in silicon solar cell technology. Rear-passivated CIGS cells have been proposed with nano-sized point contacts [16], and recently ZnS nano-dots as a passivation film in combination with In_2S_3 point contacts have proven to be a viable strategy to improve the cell performance beyond that of simple planar In_2S_3 buffer by reducing the region of high interface recombination [17]. With the passivation layer approach the requirements of buffer/absorber interface quality can be relaxed, provided that the passivation layer effectively reduces the defective junction and interface recombination losses.

Surface passivation can be used to suppress recombination, whereby the open circuit voltage and the efficiency can be improved. Passivation can lower recombination losses in two ways: i) by reducing the density of active interface defects, impurities or dangling bonds at the CIGS surface (chemical passivation); ii) the presence of charge inside the passivation layer can either repel minority carriers from the semiconductor interface (in the case of negative passivation charge) or enhance surface inversion of the CIGS (in the case of positive passivation charge), thus inhibiting recombination (field-effect passivation) [18]. In the case of silicon technologies, over the years different materials as silicon nitride (SiN), silicon dioxide (SiO_2), amorphous silicon (a-Si), and, more recently, aluminum oxide (Al_2O_3) and hafnium oxide (HfO_2), have proven to possess both chemical and field-effect passivation qualities [19–21].

Among deposition methods, atomic layer deposition, ALD, has the ability to deposit ultrathin layers down to 5 nm, at the same time maintaining good passivation of the surface [19]. The passivation capability of ALD Al_2O_3 is confirmed also when deposited on CIGS [22], probably due to the field-effect more than the reduction of defects at the surface (which is estimated at about 35%) [23]. The control of this field-effect due to charge inside the passivation layer is thus crucial to assure effective surface passivation. Even if the residual charge inside the ALD Al_2O_3 is negative, both its magnitude and polarity can be varied from -3.5×10^{12} cm^{-2} to $+4.0\times10^{12}$ cm^{-2} by inserting additional layers of HfO_2 and SiO_2 [21], making this material an interesting candidate to passivate both the front and rear sides of the absorber, where positive and negative charge, respectively, is optimum for field-effect passivation.

As far as point contact opening is concerned, unfortunately, the conventional patterning techniques used in silicon solar cells are not applicable to chalcopyrite thin films, due to the surface roughness of the polycrystalline absorber and the shorter diffusion length of minority carriers, which requires mean size and distance of localized openings in the nanometer scale [22,24,25]. Recently, though, a novel surface nanopatterning method was presented, obtained by self-assembling of alkali condensates (SALT) [26] forming nanostructures (< 30 nm) on the rough polycrystalline surface of chalcogenide thin films with conformal coverage, thus opening new opportunities for front interface passivation.

The evidence from all these studies suggests the importance of theoretical investigation of the passivation and point contacts geometry to understand their effects on cell performance, with the aim at overcoming the limitations induced by non-optimal interface properties. In this paper therefore we expand on a previous report [27] using three-dimensional (3D) numerical simulations to study the impact of inserting a passivation layer with point contacts at the buffer/CIGS interface. We vary the passivation layer thickness, and the point contact width and pitch, in order to determine the optimum configuration for high efficiency in the presence of highly defective buffer/absorber and passivation/absorber interfaces. The effect of varying the doping of CdS and CIGS in combination with point contacts is also addressed. In this study, we take a closer look at the field-effect passivation induced by the density of fixed charge inside the passivation layer. We mostly focus on a standard CdS/CIGS stack, but results are extended to different buffer materials. Moreover, since the polycrystalline structure of CIGS and the presence of gran boundaries (GBs) are known to influence the cell performance significantly [28,29], although the bulk of this work is focused on single-crystal structures, we also simulate cells featuring surface passivation and contacts openings in the presence of GBs.

The ultimate goal of this work is providing cell manufacturers with guidelines for high-efficiency designs with optimized cross-sectional and layout features, and passivation layer requirements.

2. Materials and methods

Starting from the passivation-plus-local opening geometry achievable by the SALT technique, a picture of which is shown in Fig. 1 (left) (a detailed description of the technique can be found in [26]), we simulated the cell schematically shown in Fig. 1 (right).

The passivation layer thickness h, the point contact width wpc, and pitch d are varied in order to evaluate their effect on cell performance. When h=0, the CdS covers the whole CIGS surface, and the cell structure is the standard one (i.e., with neither passivation nor point contacts).

We modeled the cells using the Synopsys Sentaurus-Tcad suite [30], using cylindrical-symmetry 3D simulations except where otherwise noted. The cell's behavior in the dark is described by the Poisson, electron and hole continuity, and drift-diffusion equations. Recombination via deep defects follows the Shockley – Read – Hall

(SRH) model. The cell is illuminated by the standard AM1.5G solar spectrum, and the light propagation through the layered media is calculated by the transfer matrix method (TMM). This model assumes ideal, flat interfaces between layers and coherent propagation, i.e., layers that are thinner than the optical coherence length. The second assumption is generally accurate enough; the first one, on the other hand, is questionable in the case of thin-film polycrystalline cells: however, since measured optical coefficients are used in the simulations, the effect of surface roughness is to some extent incorporated in the model, and TMM simulations were shown to provide good match between measured and simulated External Quantum Efficiencies (EQEs) without any fitting of optical coefficients (see for example [31]). The simulated cell has a double graded [Ga]/([Ga]+[In]) (GGI) composition of the absorber of the type described in [32], yielding a depth-dependent bandgap: the measured GGI profiles are loaded into the model of the solar cell to give the corresponding band gap profiles (as described more in detail in [31]). The optical behavior is described by complex refractive indexes coming from the literature [33] or from unpublished measured data (for CIGS), depending on both GGI and [Cu]/([Ga]+[In]) ratios. All simulations include spatially uniform bulk recombination centers in the CIGS; as far as interface recombination is concerned, we examined two scenarios for the CdS/CIGS interface: ideal interface (no trap centers), and non-ideal interface (with trap centers). While most of the simulations do not consider the presence of grain-boundaries (GBs), the effect of defect-rich GBs is considered at the end of the next section. The most significant material parameters [28,29,34] for the various cell layers are given in Table 1. The passivation is modeled as a transparent layer with Eg=5 eV, forming a conduction band spike (ΔE_C=0.5 eV) at the interface with CIGS. It is worth pointing out that the exact value of the energy gap of the passivation layer used in simulation is not very relevant, since passivation is considered to be transparent. Possible candidates for cell fabrication could be HfO_2 (Eg=5.3–5.7 eV), Al_2O_3 (Eg=6.4 eV) [35], or SiO_2 (Eg=3.9 eV), as explained later.

Table 1
Material parameters used in the simulations.

	ZnO	CdS	CIGS
E_g (eV)	3.3	2.4	graded
$N_{D/A}$ (cm^{-3})	N_D: 10^{20} - AZO N_D: 10^{17} - i-ZnO	N_D: $2{\cdot}10^{16}$	N_A: 10^{16}
$\varepsilon/\varepsilon_0$	9	9	10
Nc (cm^{-3})	2.27×10^{18}	2.27×10^{18}	0.68×10^{18}
Nv (cm^{-3})	3.34×10^{19}	1.80×10^{19}	1.53×10^{19}
μ_e (cm^2/(V s))	100	100	100
μ_h (cm^2/(V s))	25	25	25
ΔEc (eV)	−0.2	0.3	
τ_e (ns)	10	33	150
τ_h (ns)	0.01	0.01	150

Non ideal CdS/CIGS interface

Defects	N_T (cm^{-2})	Trap Energy, E_T (eV)	$\sigma_e=\sigma_h$ (cm^2)
Acceptor	$10^{10}/10^{11}$	midgap	10^{-14}
Donor	$10^{10}/10^{11}$	midgap	10^{-14}
Neutral recombination center	10^5	midgap	10^{-8}
Negatively charged defects	10^{11}	midgap	10^{-18}

CIGS grain boundary: donor-type defects

N_{DT} (cm^{-3})	E_T (eV)	$\sigma_e=\sigma_h$(cm^2)	$\Delta Ev_{(GB/GI)}$ (meV)
I) 5×10^{19}	midgap	2×10^{-15}	150
II) 5×10^{17}	midgap	2×10^{-15}	150

3. Results and discussion

3.1. CdS/CIGS cell simulation

3.1.1. Chemical passivation

We started setting the baseline for the standard cell with h=0 – i.e., no passivation – in the case of ideal CdS/CIGS interface; the simulated cell efficiency under AM1.5G illumination is 21.6%, as reported in Table 2 together with measured data from [1].

Donor-type interface states (related to $(In, Ga)_{Cu}$ defects), which can be converted from shallow to deep donors under photoexcitation [36] and deep bulk acceptor-type defects (related to the V_{Se}–$V_{Cu}^{-/2-}$ vacancy complex) crossing the Fermi-level very close to the interface are expected inside the CIGS [37] and are often associated with the N1 level observed in the admittance spectra and with light- and bias-induced metastabilities [38].

Starting from the ideal-case bulk-limited cell (η=21.6%), in order to simulate a case of surface-limited cell, we introduced either acceptor or donor traps with a density of $10^{10}\div10^{11}$ cm^{-2} at the CdS/CIGS interface, corresponding to surface recombination velocity of $10^3\div10^4$ cm/s. All traps are energetically located at the CIGS mid-gap: in fact, our simulations showed that the effect of both interface acceptor-like and donor-like defects is largely independent of the trap energy level as long as the latter is within ± 0.3 eV from the intrinsic Fermi level. As listed in Table 2, the lowest efficiency, η=15.9%, is obtained for acceptor defects of density $N_{AT}=10^{11}$ cm^{-2}, due a larger reduction of both V_{oc} and FF caused by enhanced surface recombination and defect-induced band bending.

In order to decouple the effect of recombination from that of band bending due to charged interface defects, we also simulated the separates cases of i) neutral recombination centers and ii) negatively charged (i.e., acceptor-type) interface defects with low enough capture cross section to make surface recombination negligible, as detailed in Table 2. As expected, the negatively charge defects affect FF (−2.7% absolute) due to a change in the band bending, leaving V_{oc} unchanged, while the neutral recombination centers reduce V_{oc} (−0.07 V) and, as a consequence, FF, as reported in Table 2. In the presence of acceptor traps, these two effects, namely, the different band bending due to negatively-charged acceptors and trap-assisted surface recombination, combine to reduce the cell's efficiency to the 15.9% minimum observed in Table 2.

With reference to the interface-limited cell with 10^{11} cm^{-2} acceptors, in order to identify the optimum passivation layer thickness and

Table 2
Baseline (h=0) cell parameters under AM1.5G illumination. In the case of non-ideal interface cell, A (D) indicates acceptor (donor) traps.

	N_T (cm^{-2})	V_{oc} (V)	J_{sc} (mA/cm^2)	FF (%)	η (%)
Reference: Simulated (ideal interface)		0.74	35.6	82.1	21.6
	D - 10^{11}	0.67	35.3	80.0	18.9
	D - 10^{10}	0.72	35.3	81.3	20.7
	A - 10^{11}	0.59	35.3	75.9	15.9
	A - 10^{10}	0.72	35.3	81.0	20.5
	Neutral defects	0.67	35.3	80.0	18.9
	Negatively charged defects - 10^{11}	0.74	35.3	79.4	20.7
Measurement [1]		0.74	35.1	78.9	20.4

Table 3
Cell parameters under AM1.5G illumination.

Non – ideal interface ($N_{AT}=10^{11}$ cm^{-2}) optimum wpc=20 nm and optimum d=50 nm				
h (nm)	**V_{oc} (V)**	**J_{sc} (mA/cm^2)**	**FF (%)**	**η (%)**
5	0.70	35.5	78.1	19.3
10	0.69	35.5	76.7	18.7
25	0.66	35.4	72.5	16.9

point contact layout that give the largest efficiency recovery we simulated structures (see Fig. 1, right) with different passivation thickness: h=5 nm, 10 nm, 25 nm (values compatible with ALD technique). For each value of h, we considered three values of the point contact pitch d: 50 nm, 100 nm, and 250 nm. Moreover, for each combination of h and d, we varied the point contact width wpc between 5 nm and (d – 10 nm).

The best performance, with η=19.3%, is reached with a point contact width wpc=20 nm and closely spaced (d=50 nm) point contacts. The best efficiency obtained for each value of h and the corresponding combination of d and wpc is shown in Table 3. The complete set of the cell's figures-of-merit is shown as a function of wpc and for different values of d, in the case of h=10 nm, in Fig. 2.

Even with the optimal configuration (h=5 nm, Table 3), the efficiency recovery - about 3.4% absolute – offered by surface passivation with point contacts does not restore the ideal bulk-limited case efficiency (η=21.6%). In fact, contrary to V_{oc}, which completely recovers the loss due to the defective CdS/CIGS interface, the fill factor (78.1%) remains lower than that of the ideal-interface solar cell (82.1%). As shown by Fig. 2 (top right), FF is severely degraded for narrow point contacts, due to the increased resistance of the current path in the absorber and through the point contact openings, despite the carrier diffusion length being in the micrometer range for both electrons and holes. The parasitic resistance of point contacts increases with passivation thickness, too, because the CdS thickness covering the point contact corners – which is equal to (30 nm – h), as seen in Fig. 1 - is reduced for higher h.

On the other hand, Fig. 2 shows that, starting from wpc values in the low nanometer range, increasing wpc makes the cell tend toward the surface-limited case, due to insufficient passivation of the interface defects. The performance degradation for increasing wpc can be expected to be gentler for less defective interfaces. This means that the success of the passivation-with-point-contacts strategy depends on the trade-off between the beneficial effect of surface defects passivation, which is maximum for narrow point contacts and wide pitch, and the detrimental effect of series resistance, which is aggravated when the point contacts are narrower and wider apart.

Since the series resistance introduced by the passivation layer with point contacts is the factor limiting the cell performance, we evaluated the effect of increasing the doping densities. It can be expected that the more conductive the CIGS and CdS layers, the less will the cell suffer from series resistance effects, thus enhancing the benefit of point contacts. With reference to a cell with h=10 nm, d=50 nm, wpc=10 nm, we have thus simulated the illuminated behavior for different values of the CIGS acceptor doping density keeping the CdS donor doping density fixed at 2×10^{16} cm^{-3}, and similarly for different values of CdS donor doping keeping the CIGS acceptor density fixed at 1×10^{16} cm^{-3}, as shown in Fig. 3. While increasing the CdS doping (Fig. 3, black line) does prove successful owing to reduction of the parasitic series resistance of the point contact path and improved band alignment [39], higher CIGS doping (Fig. 3, orange line) lowers the FF due to an unfavorable combination of doping and band alignment, as detailed in [27,39]. In both cases, the effect of increased doping is marginal on V_{oc} and J_{sc}, and FF controls the cell performance.

The presence of passivation on top of the CIGS makes the CdS redundant outside of the point contact areas, and suggests the possibility of removing the CdS everywhere except in the point contacts, thus increasing the photon inflow and the External Quantum Efficiency (EQE). Thus, we chose the cell with h=10 nm, wpc=10 nm, d=50 nm, and removed the CdS from the passivation top, leaving everything else unchanged. The simulated efficiency improves

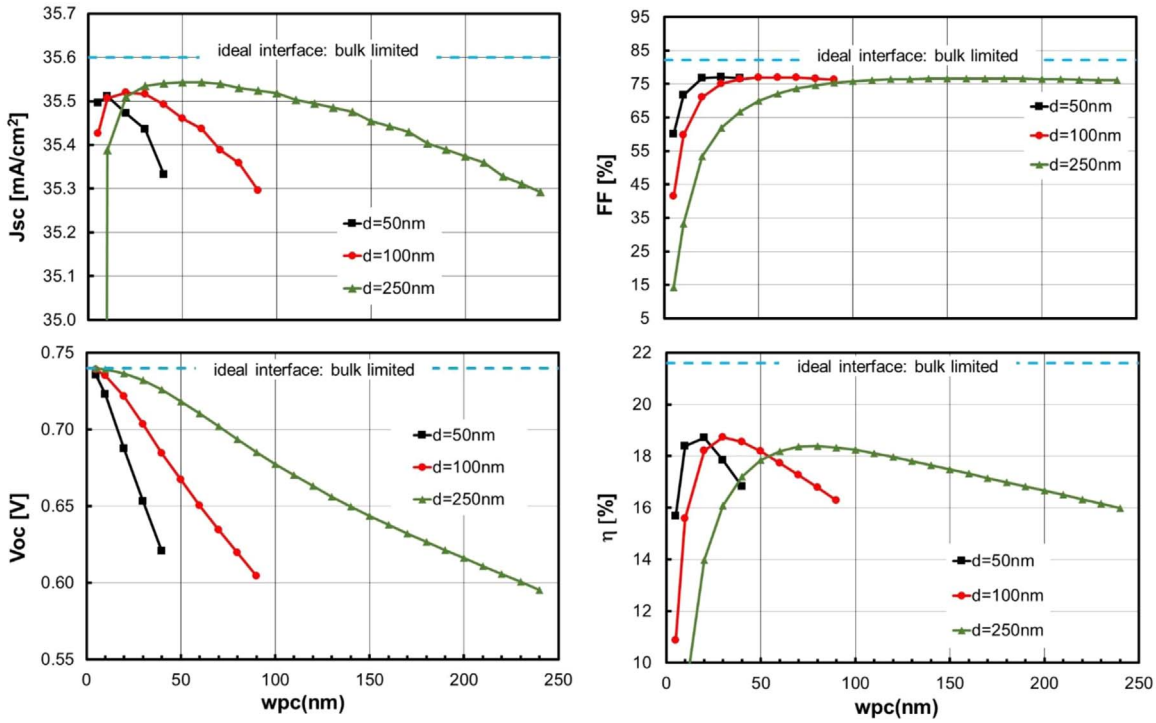

Fig. 2. Simulated cell parameters vs. point contact width, wpc, for varying pitch, d. Non-ideal interface. h=10 nm. The reference line indicates the case of absence of interface states and passivation (i.e., reference cell in Table 2).

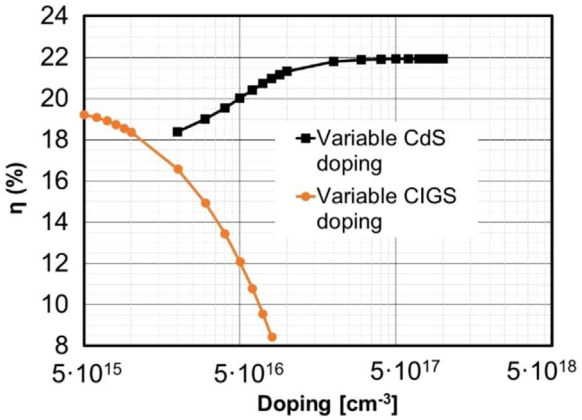

Fig. 3. Simulated efficiency versus either CIGS acceptor doping density (orange line), or CdS donor doping density (black line). Non-ideal interface (N_{AT}=10^{11} cm^{-2}). *h*=10 nm, *d*=50 nm, *wpc*=10 nm. (For interpretation of the references to color in this figure legend, the reader is referred to the web version of this article.).

from 18.4% to 21.0%, not only due the expected reduction of absorption losses in the CdS (corresponding to a J_{sc} increase of +1 mA/cm^2), but also to the improvement of FF (+7% absolute), the latter mainly attributed to the series resistance (extracted from the slopes of the I-V curve near V_{oc}) decreasing from 3.10 to 1.55 Ω cm^2 when the CdS is removed from the top of the passivation layer and is replaced by more conductive ZnO.

3.1.2. Field-effect passivation

In the previous analysis we assumed perfect passivation of interface defects, that is, defect-free passivation-layer/absorber interface. In that case the passivation with point contact arrangement allows to recover the cell efficiency significantly, but not so much as to attain the bulk-limited η=21.6%. An other cause that may lower recombination at the CIGS surface is the reduction of the density of one type of carrier by means of the electric field induced by the charge within the passivation. A positive charge, attracting electrons at the surface, favors the photocurrent flow and moves the CIGS surface deeper into inversion thus reducing the recombination. In order to evaluate this effect, we consider the presence of a fixed positive charge density, Q_f, inside the passivation layer, which is varied in the range 10^{10}–10^{13} cm^{-2}. Positive Q_f are reported in HfO_2 layers [20], in $SiO_2/HfO_2/Al_2O_3$ stacks depending on the thicknesses of different materials [21], or in as-deposited Al_2O_3 [40].

We examined two scenarios for the case of the most detrimental acceptor traps density, N_{AT}=10^{11} cm^{-2} (see Table 1 for defect properties): i) the acceptor traps are present only at the buffer/absorber interface, i.e., only in the point contact openings, which corresponds to ideal chemical passivation at the absorber/passivation interface, and ii) acceptor traps are present all over the CIGS surface, which instead simulates the opposite case of ineffective chemical passivation.

As shown in Fig. 4, even with ideal chemical passivation of defects (red triangles), the efficiency is shown to improve by almost 3.6% absolute in the case of additional field-effect passivation induced by positive Q_f mainly by the increase of FF, slightly surpassing the bulk-limited cell with no passivation (reference dotted line in Fig. 4). In fact, the positive Q_f reduces the barrier seen by photo-generated electrons leaving the absorber, as shown in in Fig. 5a for V=0.4 V (corresponding to the Maximum Power Point, MPP, in the case of Q_f=0 cm^{-2}), and also favors the accumulation of electrons at the inverted passivation/absorber interface (Fig. 5b) thereby reducing the resistance of the current path inside the absorber: consequently, FF increases and so does efficiency. Not surprisingly, the benefit of field-effect passivation is even larger in the case of inefficient chemical passivation of defects: the 12.5% efficiency obtained with Q_f=0 jumps to 21.9%, if positive $Q_f > 5\cdot10^{11}$ cm^{-2} is present at the passivation/absorber interface (Fig. 4, circles).

The efficiency improvement is due to the increase of both V_{oc} (+180 mV) and FF (+18% absolute), respectively originating from the inhibition of recombination and the improved band alignment at the CIGS surface. The presence of field-effect passivation helps relaxing the requirements on point contact size: in the presence of positive fixed charge density Q_f=10^{12} cm^{-2}, local openings through the passivation in the range 5–20 nm practically give the same cell efficiency, as shown in Fig. 6.

3.1.3. Alternative (non-CdS) buffer layers

In order to evaluate the effectiveness of field-effect passivation in combination with buffer materials alternative to CdS, we simulated the front contact nanostructured CIGS-based solar cell of Fig. 1 (*h*=10 nm, *d*=50 nm, *wpc*=10 nm), with several buffer materials alternative to CdS. We considered the same values of layer thicknesses, doping levels, and recombination rates used for the cell with CdS of Fig. 1, mainly focusing on the effect of the different conduction band offsets (CBOs) at the hetero-interfaces. The CBOs at the ZnO/buffer and buffer/CIGS interfaces used in our simulations come from the literature and are summarized in Table 4 together with the simulated cell figures of merit for the two cases of Q_f=0 (no field-effect passivation) and Q_f=1–5·10^{12} cm^{-2} (optimum field-effect passivation). In both cases, no chemical passivation of defects is considered at the passivation/CIGS interface. For the $Zn_{1-x}Mg_xO$, we considered the case of low Mg concentration (x=0.19), as previous studies [41] showed that larger x necessitates nearly degenerate or degenerate $Zn_{1-x}Mg_xO$ to achieve good efficiency. The optical complex refractive indexes of the studied buffer materials

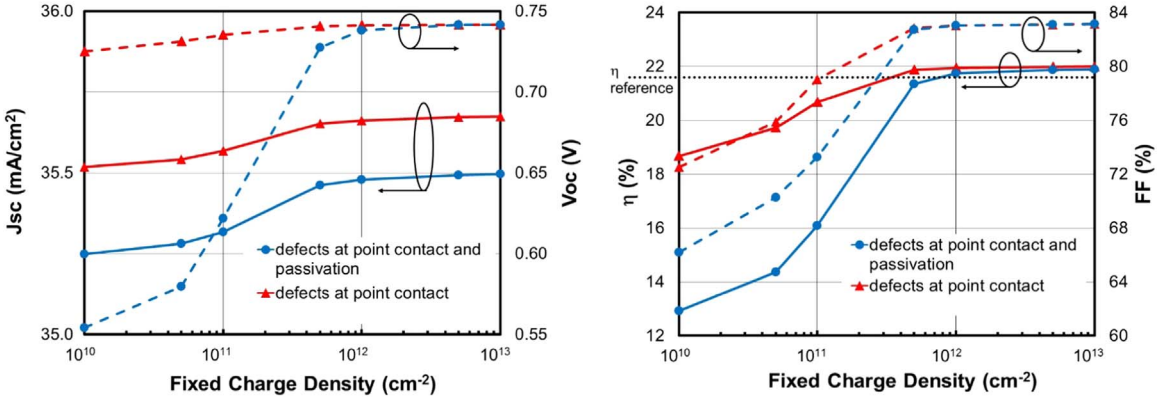

Fig. 4. Simulated cell parameters vs. fixed charge density inside the passivation layer with *h*=10 nm, *wpc*=10 nm, *d*=50 nm for the two scenarios of acceptor interface states with density 10^{11} cm^{-2} i) at point contact only (triangles) and ii) all over the CIGS surface (circles). The reference line indicates the case of absence of interface states and passivation (i.e., reference cell in Table 2).

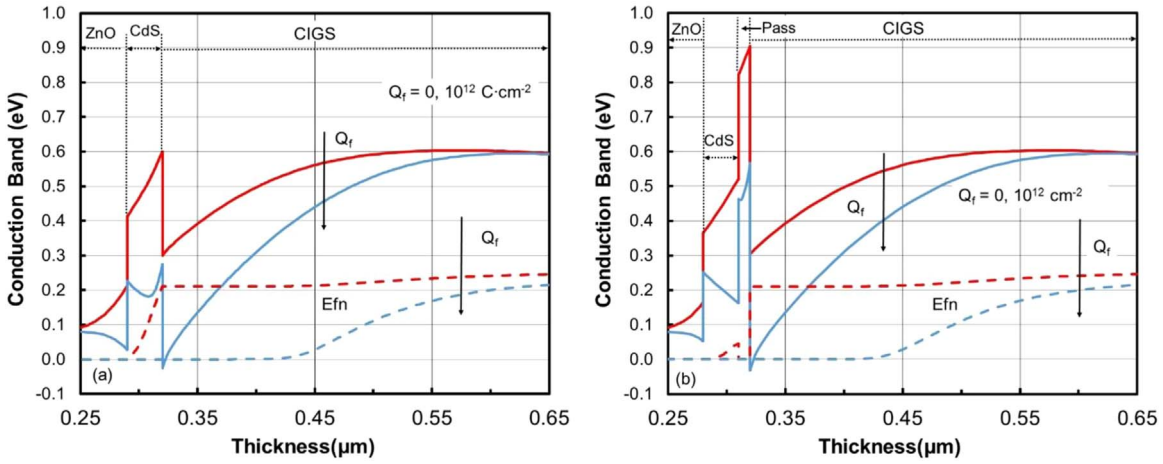

Fig. 5. Conduction band energy, E_C (solid lines) and corresponding electron Fermi energy, E_{Fn} (dashed lines) versus depth at V=0.4 V (corresponding to the MPP for the case of Q_f=0), (a) in the point contact area and (b) in the passivated area, in the case of acceptor interface states $N_{AT}=10^{11}$ cm^{-2} all over the CIGS surface and Q_f=0, 10^{12} cm^{-2}.

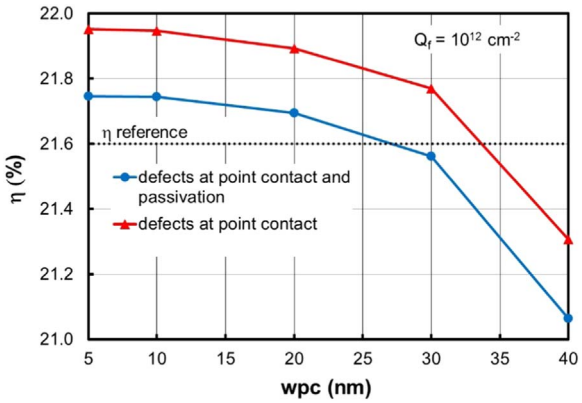

Fig. 6. Simulated cell efficiency versus point contact width, *wpc*, for the two scenarios of acceptor interface states ($N_{AT}=10^{11}$ cm^{-2}) i) at point contact only (red triangles) and ii) all over the CIGS surface (blue circles) in the case of fixed charge density $Q_f=10^{12}$ cm^{-2} inside the passivation (*h*=10 nm, *d*=50 nm). The reference line indicates the case of absence of interface states and passivation (i.e., reference cell in Table 2). (For interpretation of the references to color in this figure legend, the reader is referred to the web version of this article.).

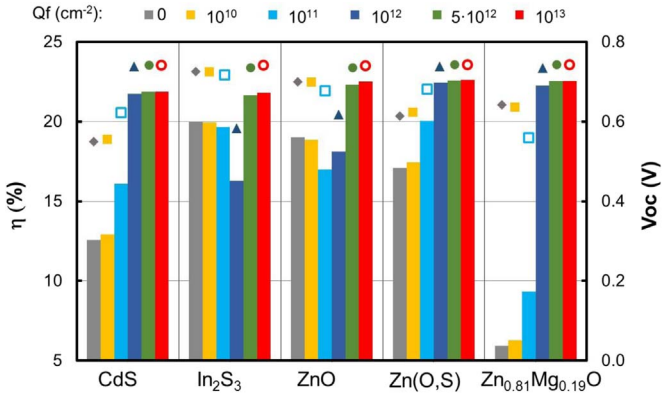

Fig. 7. Simulated cell efficiency, η, (bars) and corresponding open circuit voltage, V_{oc}, (symbols) vs. buffer material for different values of the passivation charge; *h*=10 nm, *wpc*=10 nm, *d*=50 nm. Interface acceptors, $N_{AT}=10^{11}$ cm^{-2}, are present all over the CIGS surface. In the case of Zn(O,S), S/Zn=0.28.

come from the literature (for In_2S_3) [42], from unpublished measured data (for $Zn_{0.81}Mg_{0.19}O$), or are the same as for ZnO (for the Zn(O,S)).

3.1.3.1. $CBO_{CIGS/Buffer} > 0$. As the data in Fig. 7 demonstrate, in these cases (CdS, Zn(O, S), $Zn_{0.81}Mg_{0.19}O$), a positive $Q_f \geq 10^{12}$ cm^{-2} is sufficient to hinder recombination at the defective CIGS surface for all studied materials, boosting V_{oc} (symbols) irrespective of the conduction-band offset value at the buffer/absorber hetero-junction. Moreover, the concentration of electrons, which are majority carriers at the inverted passivation/CIGS interface, is raised by the positive charge and the barrier seen by photo-generated electrons leaving the absorber

Table 4
Simulated cell performance data with and without field-effect passivation, for different buffer materials (*h*=10 nm, *wpc*=10 nm, *d*=50 nm) in the case of acceptor interface states ($N_{AT}=10^{11}$ cm^{-2}) at point contacts and passivation/absorber interface. No chemical passivation of defects is assumed at the passivation/CIGS interface. Negative (positive) CBO indicates a cliff (spike).

Solar cell stack	$CBO_{CIGS/Buffer}$ (eV)	$CBO_{Buffer/ZnO}$ (eV)	Q_f (cm^{-2})	J_{sc} (mA/cm^2)	V_{oc} (V)	FF (%)	η (%)
ZnO/i-ZnO/CdS/CIGS	0.3 [43]	−0.2 [44]	0	35.2	0.55	64.8	12.6
			10^{12}	35.5	0.74	83.0	21.7
ZnO/i-ZnO/In_2S_3/CIGS (Na containing)	−0.25 [42]	−0.2 [45]	0	33.9	0.72	81.1	19.9
			$5{\cdot}10^{12}$	35.4	0.73	83.1	21.6
ZnO/i-ZnO/ZnO/CIGS	−0.2 [44]	0	0	36.0	0.70	75.3	19.0
			$5{\cdot}10^{12}$	36.6	0.73	83.1	22.3
ZnO/i-ZnO/Zn(O,S)/CIGS, S/Zn=0.28	0.2 [46]	0 [47]	0	36.4	0.61	76.4	17.1
			10^{12}	36.6	0.74	83.1	22.5
ZnO/i-ZnO/$Zn_{0.81}Mg_{0.19}O$/CIGS	0.2 [44]	−0.35 [48]	0	36.0	0.64	25.5	5.9
			10^{12}	36.5	0.73	83.0	22.3

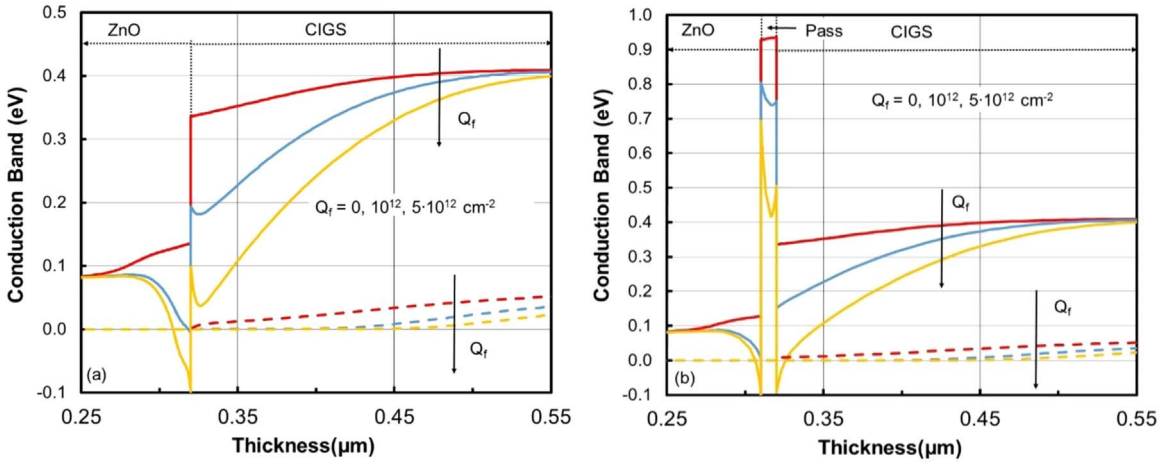

Fig. 8. Conduction band energy, E_C (solid lines) and corresponding electron Fermi energy, E_{Fn}, (dashed lines) versus depth at V=0.59 V (corresponding to the MPP for the case of Q_f=0), (a) in the point contact area and (b) in the passivated area, in the case of acceptor interface states with density 10^{11} cm^{-2} all over the CIGS surface (circles) and Q_f=0, 10^{12}, $5{\cdot}10^{12}$ cm^{-2}.

is reduced (see Fig. 5b), so that the FF monotonically increases with Q_f. The combination of the two factors leads the efficiency (bars in Fig. 7) up to and beyond 21.6%.

3.1.3.2. $CBO_{CIGS/Buffer} < 0$. In the presence of a cliff at the buffer/CIGS interface (In_2S_3/ZnO), the barrier to the flow of photo-generated electrons from the absorber to the buffer layer is removed, as shown by conduction band diagram of ZnO-buffered cell depicted in Fig. 8a, and FF is higher than that of $CBO_{CIGS/Buffer} > 0$ case, even when Q_f=0, and increases further with positive Q_f due to the increased band-bending under the point-contact (Fig. 8a) and passivation (Fig. 8b), the latter mainly reducing the series resistance of the current path.

As the positive Q_f increases, the downward band-bending of the conduction band enhances the interface acceptor trap ionization and at the same time repels holes (minority carriers) at the surface: the competing effects of increased inversion (hindering recombination) and enhanced trap ionization (promoting recombination) determine the non-monotonic V_{oc} dependence on the fixed charge density, as shown by data in Table 5. The high V_{oc} and FF when Q_f=0 combine to give the 19% efficiency of the ZnO/i-ZnO/CIGS stack (19.9% for ZnO/i-ZnO/In_2S_3/CIGS). In the case of ZnO (In_2S_3) buffer, the minimum V_{oc} is reached for Q_f=10^{12} cm^{-2}, beyond which the electric field induced by Q_f is high enough to push away the holes from the CIGS surface; the recombination decreases again and V_{oc} starts to increase like for the other buffer materials boosting the efficiency to 22.3% for ZnO and 21.6% for In_2S_3.

Table 5
Ionized interface acceptors density N_{AT}^-, recombination velocity at CIGS surface and Voc in the case of ZnO-buffered cell for different values of the passivation charge. *h*=10 nm, *wpc*=10 nm, *d*=50 nm and interface acceptors N_{AT}=10^{11} cm^{-2} all over the CIGS surface at V=0.59 V (corresponding to the MPP for the case of Q_f=0).

Q_f (cm^{-2})	N_{AT}^-, Ionized trap density (cm^{-2})		Recombination (cm^{-2} s^{-1})		V_{oc} (V)
	@ Passivation/ CIGS interface	@ ZnO/ CIGS interface	@ Passivation/ CIGS interface	@ ZnO/ CIGS interface	
0	$1.9{\cdot}10^7$	$1.45{\cdot}10^7$	$2.1{\cdot}10^{16}$	$1.6{\cdot}10^{16}$	0.7
10^{12}	$9.9{\cdot}10^{10}$	$9.0{\cdot}10^{10}$	$9.3{\cdot}10^{16}$	$3.7{\cdot}10^{17}$	0.61
$5{\cdot}10^{12}$	10^{11}	10^{11}	$2.8{\cdot}10^{13}$	$1.2{\cdot}10^{16}$	0.73

3.2. Poly-crystalline cell simulation

Even if polycrystalline CIGS solar cells have reached efficiencies up to 22.6% [2], the presence of grain boundaries (GBs) is detrimental to the efficiency, as shown in many studies [28,29,49,50]; therefore, we analyzed the effect of the presence of GBs in a cell with passivation and contact openings, as shown in Fig. 9.

In this case, due to the great number of grid points required to model such a wide area with the necessary resolution and the absence of the cylindrical symmetry of the structure in Fig. 1, we performed 2D simulations (as opposed to the 3D simulations described so far). Even if the simulated contact openings represent line contacts rather than point contacts, the simulation study can give an indication of the effects of GB in the presence of a nanostructured CIGS front surface. In order to simulate a realistic structure, we considered a grain size of 750 nm containing 15 line contacts with 50 nm pitch, and *wpc*=10 nm. We also varied the distance t of the GB relative to contact center (t=0 and 20 nm). Thanks to symmetry, we modeled only half of the structure in Fig. 9, for the two cases where the GB lies i) exactly in the middle of at the contact opening (as shown in Fig. 9), or ii) midway between neighboring point contacts. We considered the case of ideal chemical passivation of defects (i.e., defects at point contact only) and no field-effect passivation (i.e, Q_f=0).

The GB is modeled by a 2 nm wide region rich with donor traps [28,51] (see Table 1 for GB trap parameters): we considered both the cases of high (N_T=10^{13} cm^{-2}, which corresponds to $5{\cdot}10^{19}$ cm^{-3}) and

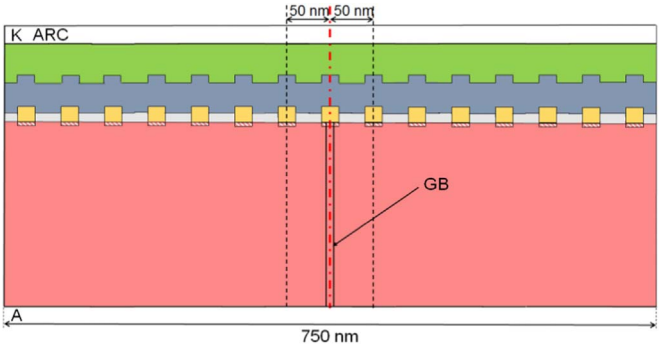

Fig. 9. Structure of a cell with a 750 nm wide grain with 15 contacts openings and a grain boundary (GB). The 2-nm wide GB area is rich with donor traps while acceptor defects (N_{AT}=10^{11} cm^{-2}) are distributed at the CdS/CIGS interface (red-hatched region), as detailed in Table 1. Thanks to symmetry, only half of the structure has been simulated. No fixed charge is assumed within the passivation layer. (For interpretation of the references to color in this figure legend, the reader is referred to the web version of this article.).

Table 6
Cell parameters under AM1.5G illumination for the cell in Fig. 9, in the case of a GB in the middle of a contact opening. 2D simulations.

Structure		V_{oc} (V)	J_{sc} (mA/cm^2)	FF (%)	η (%)
No GB		0.7	36.5	80.6	20.8
GB	I)	0.7	36.3	78.6	19.9
	II)	0.7	36.5	80.6	20.8

low (N_T=10^{11} cm^{-2}, which corresponds to $5{\cdot}10^{17}$ cm^{-3}) defect density inside GBs. Besides the different defect population, the GB differs from the grain interior (GI), by a larger bandgap due to Cu depletion; the band discontinuity is entirely in the valance band, and we assumed $\Delta Ev_{(GB/GI)}$=0.15 eV [52–54].

In the presence of the most defective GBs (type I in Tables 1 and 6), the cell efficiency is reduced by about 1%, mainly by the drop of FF, while the GB position relative to the contact center does not affect the obtained results. So, there appears to be no significant interaction of GBs with the passivation and point contact scheme, and the single-crystal results shown above can be considered to be representative.

4. Conclusions

This work details the application of 3D numerical simulation to the optimization of CIGS solar cells with passivated buffer/absorber interface and front-side point contacts. The effects of both chemical and field-effect passivation are analyzed in the case of CdS as well as alternative buffer materials.

We found that, in the presence of surface-limited performance – i.e., with strongly defective buffer/CIGS interface – the use of surface passivation in combination with point contacts can help the cell recover most of the performance loss due to interface states, provided that the passivation is effective in removing the surface defects (i.e., good or ideal chemical passivation of defects). Nanometer-scale point contact openings with pitch of a few tens of nanometers give the best results for the structures we considered. We identified the fill factor as the main performance bottleneck and showed that lower series resistances (leading to higher fill factor), can be obtained with thin passivation layer and high doping density (≥10^{17} cm^{-3}) of buffer layer, but also removing the CdS from the top of the passivation.

Simulations of the CdS-buffered cell showed that positive charge in the order of 10^{12} cm^{-2} within the passivation can improve the efficiency of a cell with ideal chemical passivation by about 3.4% absolute, mainly thanks to better fill-factor. This field-effect passivation is even more effective in the case of inefficient chemical passivation. The positive charge also helps relaxing the requirements on the point contact geometry: point contact widths up to 20 nm can be used without significant efficiency loss.

Front contact nanostructured CIGS-based solar cells with different buffer layers (Zn(O,S), ZnO, $Zn_{0.81}Mg_{0.19}O$, In_2S_3) have also been simulated, demonstrating that when the positive charge within the passivation is sufficiently high (in the range 10^{12}–$5{\cdot}10^{12}$ cm^{-2}), the benefit of field-effect passivation also applies to cells having unfavorable conduction-band offset (i.e., cliff or low spike) at the buffer/CIGS interface, yielding efficiencies over 21% for all samples, and allowing more flexibility in the choice of the buffer layer.

Finally, it is worth pointing out that the efficiency ceiling (21.6%) shown by the simulated cells of this work is determined by the choice of the baseline structure, and is not an intrinsic limitation of the passivation/point contact process: under favorable conditions of chemical and field-effect passivation, an optimized front nanostructure can recover the efficiency loss due to interface recombination, boosting the efficiency to the value which is obtained when the bulk properties are limiting the cell performance.

Acknowledgements

This project has received funding from the European Union's Horizon 2020 research and innovation programme under grant agreement No 641004, project Sharc25.

This work was also supported by the Swiss State Secretariat for Education, Research and Innovation (SERI) under contract number REF-1131-52107.

References

[1] A. Chirilă, P. Reinhard, F. Pianezzi, P. Bloesch, A.R. Uhl, C. Fella, L. Kranz, D. Keller, C. Gretener, H. Hagendorfer, D. Jaeger, R. Erni, S. Nishiwaki, S. Buecheler, A.N. Tiwari, Potassium-induced surface modification of Cu(In,Ga)Se2 thin films for high-efficiency solar cells, Nat. Mater. 12 (2013) 1107–1111. http://dx.doi.org/10.1038/nmat3789.

[2] P. Jackson, R. Wuerz, D. Hariskos, E. Lotter, W. Witte, M. Powalla, Effects of heavy alkali elements in Cu(In,Ga)Se $_2$ solar cells with efficiencies up to 22.6%, Phys. Status Solidi - Rapid Res. Lett. 586 (2016) 583–586. http://dx.doi.org/10.1002/pssr.201600199.

[3] K. Rui, Y. Takeshi, A. Shunsuke, H. Atsushi, F.T. Kong, K. Takuya, S. Hiroki, New world record Cu(In,Ga)(Se,S)2 thin film solar cell efficiency beyond 22%, in: Proceedings of the IEEE 43th Photovolt. Spec. Conference PVSC 2016 Portland(OR) USA, June 2016, pp. 3–7.

[4] R. Klenk, Characterisation and modelling of chalcopyrite solar cells, Thin Solid Films 387 (2001) 135–140. http://dx.doi.org/10.1016/S0040-6090(00)01736-3.

[5] T. Minemoto, T. Matsui, H. Takakura, Y. Hamakawa, T. Negami, Y. Hashimoto, T. Uenoyama, M. Kitagawa, Theoretical analysis of the effect of conduction band offset of window/CIS layers on performance of CIS solar cells using device simulation, Sol. Energy Mater. Sol. Cells 67 (2001) 83–88. http://dx.doi.org/10.1016/S0927-0248(00)00266-X.

[6] V. Nadenau, U. Rau, A. Jasenek, H.W. Schock, Electronic properties of CuGaSe2-based heterojunction solar cells. Part I. Transport analysis, J. Appl. Phys. 87 (2000) 584–593. http://dx.doi.org/10.1063/1.371903.

[7] R. Scheer, Activation energy of heterojunction diode currents in the limit of interface recombination, J. Appl. Phys. 105 (2009). http://dx.doi.org/10.1063/1.3126523.

[8] P. Reinhard, B. Bissig, F. Pianezzi, E. Avancini, H. Hagendorfer, D. Keller, P. Fuchs, M. Döbeli, C. Vigo, P. Crivelli, S. Nishiwaki, S. Buecheler, A.N. Tiwari, Features of KF and NaF postdeposition treatments of Cu(In,Ga)Se 2 absorbers for high efficiency thin film solar cells, Chem. Mater. 27 (2015) 5755–5764. http://dx.doi.org/10.1021/acs.chemmater.5b02335.

[9] N. Naghavi, D. Abou-Ras, N. Allsop, N. Barreau, S. Bücheler, A. Ennaoui, C.H. Fischer, C. Guillen, D. Hariskos, J. Herrero, R. Klenk, K. Kushiya, D. Lincot, R. Menner, T. Nakada, C. Platzer-Björkman, S. Spiering, A.N. Tiwari, T. Törndahl, Buffer layers and transparent conducting oxides for chalcopyrite Cu(In,Ga)(S,Se)2 based thin film photovoltaics: present status and current developments, Prog. Photovolt. Res. Appl. 18 (2010) 411–433. http://dx.doi.org/10.1002/pip.955.

[10] T. Kobayashi, T. Kumazawa, Z. Jehl Li Kao, T. Nakada, Cu(In,Ga)Se2 thin film solar cells with a combined ALD-Zn(O,S) buffer and MOCVD-ZnO:B window layers, Sol. Energy Mater. Sol. Cells 119 (2013) 129–133. http://dx.doi.org/10.1016/j.solmat.2013.05.052.

[11] M. Nakamura, N. Yoneyama, K. Horiguchi, Y. Iwata, K. Yamaguchi, H. Sugimoto, T. Kato, Recent R & D progress in solar frontier's small-sized Cu(InGa)(SeS)2 solar cells, in: Proceedings of the IEEE 40th Photovolt. Spec. Conference PVSC, 2014, pp. 107–110. http://dx.doi.org/10.1109/PVSC.2014.6925346.

[12] J. Lindahl, J.T. Wätjen, A. Hultqvist, T. Ericson, M. Edoff, T. Törndahl, The effect of Zn1-xSnxOy buffer layer thickness in 18.0% efficient Cd-free Cu(In,Ga)Se2 solar cells, Prog. Photovolt. Res. Appl. 21 (2013) 1588–1597. http://dx.doi.org/10.1002/pip.2239.

[13] A. Niemegeers, M. Burgelman, A. De Vos, On the CdS/CuInSe2 conduction band discontinuity, Appl. Phys. Lett. 67 (1995) 843. http://dx.doi.org/10.1063/1.115523.

[14] S. Siebentritt, What limits the efficiency of chalcopyrite solar cells?, Sol. Energy Mater. Sol. Cells 95 (2011) 1471–1476. http://dx.doi.org/10.1016/j.solmat.2010.12.014.

[15] Z. Wang, P. Han, H. Lu, H. Qian, L. Chen, Q. Meng, N. Tang, F. Gao, Y. Jiang, J. Wu, W. Wu, H. Zhu, J. Ji, Z. Shi, A. Sugianto, L. Mai, B. Hallam, S. Wenham, Advanced PERC and PERL production cells with 20.3% record efficiency for standard commercial p-type silicon wafers, Prog. Photovolt. Res. Appl 20 (2012) 260–268. http://dx.doi.org/10.1002/pip.2178.

[16] B. Vermang, V. Fjällström, J. Pettersson, P. Salomé, M. Edoff, Development of rear surface passivated Cu(In,Ga)Se2 thin film solar cells with nano-sized local rear point contacts, Sol. Energy Mater. Sol. Cells 117 (2013) 505–511. http://dx.doi.org/10.1016/j.solmat.2013.07.025.

[17] Y. Fu, N.A. Allsop, S.E. Gledhill, T. Köhler, M. Krüger, R. Sáez-Araoz, U. Blöck, M.C. Lux-Steiner, C.H. Fischer, ZnS nanodot film as defect passivation layer for Cu(In,Ga)(S,Se) 2 thin-film solar cells deposited by Spray-ILGAR (ion-layer gas reaction), Adv. Energy Mater. 1 (2011) 561–564. http://dx.doi.org/10.1002/aenm.201100146.

[18] G. Dingemans, W.M.M. Kessels, Status and prospects of Al2O3-based surface passivation schemes for silicon solar cells, J. Vac. Sci. Technol. A Vac. Surf. Films

30 (2012) 40802. http://dx.doi.org/10.1116/1.4728205.
[19] G. Dingemans, M.M. Mandoc, S. Bordihn, M.C.M. van de Sanden, W.M.M. Kessels, Effective passivation of Si surfaces by plasma deposited SiOx/a-SiNx:H stacks, Appl. Phys. Lett. 98 (2011) 222102. http://dx.doi.org/10.1063/1.3595940.
[20] A. Morato, B. Vermang, H. Goverde, E. Cornagliotti, G. Meneghesso, J. John, Electrical characterization of ALD Al203 - Hf02 and PECVD Al203 passivation layers for p-type CZ-Silicon PERC solar cells, IEEE PVSC (2011) 1077–1082. http://dx.doi.org/10.1109/PVSC.2012.6317790.
[21] D.K. Simon, P.M. Jordan, T. Mikolajick, I. Dirnstorfer, On the control of the fixed charge densities in Al2O3-based silicon surface passivation schemes, ACS Appl. Mater. Interfaces 7 (2015) 28215–28222. http://dx.doi.org/10.1021/acsami.5b06606.
[22] B. Vermang, V. Fjällström, X. Gao, M. Edoff, Improved rear surface passivation of Cu(In,Ga)Se solar cells: a combination of an Al2O3 rear surface passivation layer and nanosized local rear point contacts, IEEE J. Photovoltaics 4 (2014) 486–492. http://dx.doi.org/10.1109/JPHOTOV.2013.2287769.
[23] W.-W. Hsu, J.Y. Chen, T.-H. Cheng, S.C. Lu, W.-S. Ho, Y.-Y. Chen, Y.-J. Chien, C.W. Liu, Surface passivation of Cu(In,Ga)Se2 using atomic layer deposited Al2O3, Appl. Phys. Lett. 100 (2012) 23508. http://dx.doi.org/10.1063/1.3675849.
[24] N. Allsop, R. Nürnberg, M.C. Lux-Steiner, T. Schedel-Niedrig, Three-dimensional simulations of a thin film heterojunction solar cell with a point contact/defect passivation structure at the heterointerface, Appl. Phys. Lett. 95 (2009). http://dx.doi.org/10.1063/1.3233962.
[25] A. Bercegol, B. Chacko, R. Klenk, I. Lauermann, M.C. Lux-Steiner, M. Liero, Point contacts at the copper-indium-gallium-selenide interface – a theoretical outlook, J. Appl. Phys. 119 (2016). http://dx.doi.org/10.1063/1.4947267.
[26] P. Reinhard, B. Bissig, F. Pianezzi, H. Hagendorfer, G. Sozzi, R. Menozzi, C. Gretener, S. Nishiwaki, S. Buecheler, A.N. Tiwari, Alkali-templated surface nanopatterning of chalcogenide thin films: a novel approach toward solar cells with enhanced efficiency, Nano Lett. 15 (2015) 3334–3340. http://dx.doi.org/10.1021/acs.nanolett.5b00584.
[27] G. Sozzi, D. Pignoloni, R. Menozzi, F. Pianezzi, P. Reinhard, B. Bissig, S. Buecheler, A.N. Tiwari, Designing CIGS solar cells with front-side point contacts, in: Proceedings of IEEE 42nd Photovolt. Spec. Conference, IEEE, 2015, pp. 1–5. http://dx.doi.org/10.1109/PVSC.2015.7355691.
[28] K. Taretto, U. Rau, K. Taretto, U. Rau, Numerical simulation of carrier collection and recombination at grain boundaries in Cu (In , Ga) Se2 solar cells, J. Appl. Phys. 94523 (2008). http://dx.doi.org/10.1063/1.2917293.
[29] G. Sozzi, R. Mosca, M. Calicchio, R. Menozzi, Anomalous dark current ideality factor (n > 2) in thin-film solar cells: The role of grain-boundary defects, in: Proceedings of the IEEE 40th Photovolt. Spec. Conference PVSC 2014, 2014, http://dx.doi.org/10.1109/PVSC.2014.6925252.
[30] Synopsys TCAD, ⟨http://www.synopsys.com/Tools/TCAD/Pages/default.aspx⟩.
[31] G. Sozzi, S. Di Napoli, R. Menozzi, R. Carron, E. Avancini, B. Bissig, S. Buecheler, A. N. Tiwari, Analysis of Ga grading in CIGS absorbers with different Cu content, in: Proceedings of the IEEE 43rd Photovolt. Spec. Conference, IEEE, 2016, pp. 2279–2282. http://dx.doi.org/10.1109/PVSC.2016.7750042.
[32] E. Avancini, R. Carron, B. Bissig, P. Reinhard, R. Menozzi, G. Sozzi, S. Di Napoli, T. Feurer, S. Nishiwaki, S. Buecheler, A.N. Tiwari, Impact of compositional grading and overall Cu deficiency on the near-infrared response in Cu(In, Ga)Se2 solar cells, Prog. Photovolt. Res. Appl. 25 (2017) 233–241. http://dx.doi.org/10.1002/pip.2850.
[33] T. Hara, T. Maekawa, S. Minoura, Y. Sago, S. Niki, H. Fujiwara, Quantitative assessment of optical gain and loss in submicron-textured CuIn1-xGaxSe2 solar cells fabricated by three-stage coevaporation, Phys. Rev. Appl. 2 (2014) 1–17. http://dx.doi.org/10.1103/PhysRevApplied.2.034012.
[34] R. Scheer, Towards an electronic model for CuIn1−xGaxSe2 solar cells, Thin Solid Films 519 (2011) 7472–7475. http://dx.doi.org/10.1016/j.tsf.2011.01.092.
[35] H.Y. Yu, M.F. Li, B.J. Cho, C.C. Yeo, M.S. Joo, D.-L. Kwong, J.S. Pan, C.H. Ang, J.Z. Zheng, S. Ramanathan, Energy gap and band alignment for (HfO2)(Al2O3)1−x on (100) Si, Appl. Phys. Lett. 81 (2002) 376. http://dx.doi.org/10.1063/1.1492024.
[36] S. Lany, A. Zunger, Intrinsic DX centers in ternary chalcopyrite semiconductors, Phys. Rev. Lett. 100 (2008) 1–4. http://dx.doi.org/10.1103/PhysRevLett.100.016401.
[37] S. Lany, A. Zunger, Light- and bias-induced metastabilities in Cu(In,Ga)Se[sub 2] based solar cells caused by the (V[sub Se]-V[sub Cu]) vacancy complex, J. Appl. Phys. 100 (2006) 113725. http://dx.doi.org/10.1063/1.2388256.
[38] M. Igalson, A. Urbaniak, M. Edoff, Reinterpretation of defect levels derived from capacitance spectroscopy of CIGSe solar cells, Thin Solid Films 517 (2009) 2153–2157. http://dx.doi.org/10.1016/j.tsf.2008.10.092.
[39] G. Sozzi, F. Troni, R. Menozzi, On the combined effects of window/buffer and buffer/absorber conduction-band offsets, buffer thickness and doping on thin-film solar cell performance, Sol. Energy Mater. Sol. Cells 121 (2014). http://dx.doi.org/10.1016/j.solmat.2013.10.037.
[40] R. Kotipalli, B. Vermang, J. Joel, R. Rajkumar, M. Edoff, D. Flandre, Investigating the electronic properties of Al2O3/Cu(In,Ga)Se2 interface, AIP Adv. 5 (2015). http://dx.doi.org/10.1063/1.4932512.
[41] F. Troni, G. Sozzi, R. Menozzi, A numerical study of the design of ZnMgO window layer for Cadmium-free thin-film CIGS solar cells, in: 7th Conference Ph.D. Res. Microelectron. Electron. PRIME 2011 - Conference Proceedings, 2011, pp. 193–196. http://dx.doi.org/10.1109/PRIME.2011.5966250.
[42] J. Sterner, J. Malmstrom, L. Stolt, Study on ALD In2S3Cu(In,Ga)Se-2 interface formation, Prog. Photovolt. 13 (2005) 179–193. http://dx.doi.org/10.1002/pip.595.
[43] M. Gloeckler, J.R. Sites, Efficiency limitations for wide-band-gap chalcopyrite solar cells, Thin Solid Films 480–481 (2005) 241–245. http://dx.doi.org/10.1016/j.tsf.2004.11.018.
[44] T. Törndahl, C. Platzer-Björkman, J. Kessler, M. Edoff, Atomic layer deposition of Zn1-xMgxO buffer layers for Cu(In,Ga)Se2 solar cells, Prog. Photo. Res. Appl. 15 (2007) 225–235. http://dx.doi.org/10.1002/pip.
[45] S. Khanchandani, S. Kundu, A. Patra, A.K. Ganguli, Band gap tuning of ZnO/In2S3 core/shell nanorod arrays for enhanced visible-light-driven photocatalysis, J. Phys. Chem. C 117 (2013) 5558–5567. http://dx.doi.org/10.1021/jp310495j.
[46] C. Platzer-Björkman, T. Törndahl, D. Abou-Ras, J. Malmström, J. Kessler, L. Stolt, Zn(O,S) buffer layers by atomic layer deposition in Cu(In,Ga)Se2 based thin film solar cells: band alignment and sulfur gradient, J. Appl. Phys. 100 (2006) 44506. http://dx.doi.org/10.1063/1.2222067.
[47] C. Persson, C. Platzer-Björkman, J. Malmström, T. Törndahl, M. Edoff, Strong valence-band offset bowing of ZnO1-xSx enhances p-type nitrogen doping of ZnO-like alloys, Phys. Rev. Lett. 97 (2006) 1–4. http://dx.doi.org/10.1103/PhysRevLett.97.146403.
[48] X. Li, A. Kanevce, J.V. Li, I. Repins, B. Egaas, R. Noufi, Impact of Zn1-XMnXO on Cu(In,Ga)Se2 thin-film solar cells, Conference Rec. IEEE Photovolt. Spec. Conference, 2009, pp. 000305–000308. http://dx.doi.org/10.1109/PVSC.2009.5411675.
[49] G. Sozzi, R.Menozzi, N. Cavallari, M. Bronzoni, F. Annoni, M. Calicchio, M. Mazzer, On the temperature behavior of shunt-leakage currents in Cu(In,Ga)Se2 solar cells: the role of grain boundaries and rear Schottky contact, in: Proceedings of the IEEE 42nd Photovolt. Spec. Conference PVSC 2015, 2015, http://dx.doi.org/10.1109/PVSC.2015.7355779.
[50] G. Sozzi, F. Troni, R. Menozzi, Numerical analysis of the effect of grain size and defects on the performance of CIGS solar cells, CS MANTECH Conference May 17th-20th, 2010, Portland, Oregon, USA, 2010, pp. 353–356.
[51] F. Troni, F. Dodi, G. Sozzi, R. Menozzi, Modeling of thin-film Cu(In,Ga)Se2 solar cells, in: International Conference Simul. Semicond. Process. Devices, SISPAD, 2010, http://dx.doi.org/10.1109/SISPAD.2010.5604580.
[52] C. Persson, A. Zunger, Compositionally induced valence-band offset at the grain boundary of polycrystalline chalcopyrites creates a hole barrier, Appl. Phys. Lett. 87 (2005) 1–3. http://dx.doi.org/10.1063/1.2132537.
[53] M.J. Hetzer, Y.M. Strzhemechny, M. Gao, S. Goss, M.A. Contreras, A. Zunger, L.J. Brillson, On microscopic compositional and electrostatic properties of grain boundaries in polycrystalline CuIn1-xGaxSe2, J. Vac. Sci. Technol. B Microelectron. Nanom. Struct. 24 (2006) 1739. http://dx.doi.org/10.1116/1.2209995.
[54] M. Hafemeister, S. Siebentritt, J. Albert, M.C. Lux-Steiner, S. Sadewasser, Large neutral barrier at grain boundaries in chalcopyrite thin films, Phys. Rev. Lett. 104 (2010) 14–17. http://dx.doi.org/10.1103/PhysRevLett.104.196602.